Authors Version

Estimation of CMAS Infiltration depth in EB-PVD TBCs: A new constraint model supported with experimental approach.

[a]Ravisankar Naraparaju, Juan J. Gomez Chavez[a,b], Philipp Niemeyer[a], Kai-Uwe Hess[c], Wenjia Song[c], Donald B. Dingwell[c], Siddharth Lokachari[c], C.V. Ramana[b] , Uwe Schulz[a].

[a]German Aerospace Center (DLR), Institute of Material Research, Cologne, 51170, Germany

[b]University of Texas at El Paso, Department of Mechanical Engineering, El Paso, TX, 79968, USA

[c]Ludwig-Maximilians-Universität München, Department of Earth and Environmental Sciences, Munich, 80333, Germany

Journal of the European Ceramic Society 39 (2019) 2936-2945

https://doi.org/10.1016/j.jeurceramsoc.2019.02.040

Estimation of CMAS Infiltration depth in EB-PVD TBCs: A new constraint model supported with experimental approach.

[a]Ravisankar Naraparaju, Juan J. Gomez Chavez[a,b], Philipp Niemeyer[a], Kai-Uwe Hess[c], Wenjia Song[c], Donald B. Dingwell[c], Siddharth Lokachari[c], C.V. Ramana[b] , Uwe Schulz[a].

[a]German Aerospace Center (DLR), Institute of Material Research, Cologne, 51170, Germany

[b]University of Texas at El Paso, Department of Mechanical Engineering, El Paso, TX, 79968, USA

[c]Ludwig-Maximilians-Universität München, Department of Earth and Environmental Sciences, Munich, 80333, Germany

Abstract

Two standard 7YSZ coatings were deposited by EB-PVD techniques and tested against CMAS infiltration at short time intervals (up to 8 min.) at 1250˚C in air. They exhibited different microstructures, i.e. porosities and microstructural features. Two species of CMAS with different compositions were used and their viscosities were determined using the concentric cylinder method and their contact angles were measured using high temperature heating microscopy. The theoretical viscosities, which were calculated using a statistical model based on the chemical composition of the melts, differed from the measured values of the viscosities by one order of magnitude. A large variation in the contact angles within a very short range of temperature (1243-1266°C) was observed as well. The porosity and surface area measurements were performed on both EB-PVD microstructures using the nitrogen physisorption method. Additionally, the produced coatings exhibited porosities of 14.5 and 29.5 percent and the infiltration experiments have shown that the more porous coating provides higher infiltration resistance. The effect of porosity on CMAS infiltration kinetics was investigated and the results elucidate that the porosity network plays a more preeminent role than the amount of porosity. The experimental infiltration results have been compared with calculated infiltration data using a novel mathematical approach proposed in previous studies in which the permeability of the coatings is assessed with two contrasting methods termed “concentric pipe” and “open pipe” models. The infiltration was calculated by incorporating the experimentally determined properties such as contact angle, viscosity and porosity. A fitting parameter has been derived from the equations for the geometry factor for both microstructures. The calculated and experimental results are in good agreement with the concentric pipe model supporting the validity of this CMAS infiltration model.

1. Introduction

Infiltration of silicate sand and volcanic ash yields detrimental effects on the durability and performance of 7 wt.% yttria stabilized zirconia (7YSZ) thermal barrier coatings (TBC) [1-7]. They are commonly approximated by synthetic CaO-MgO-Al_2O_3-SiO_2 (so-called CMAS) simplified analog glass melts in TBC infiltration tests [6-8]. TBCs used on rotating components such as turbine blades are deposited by electron beam physical vapor deposition (EB-PVD). They typically exhibit a columnar structure with inter-columnar gaps which provide strain tolerance upon high thermal cycling [9, 10]. When the sand or ash particles are ingested into the engines at low temperatures, they can generate TBC spallation due to foreign object impact and

erosion which yields exposure of the super-alloy components to temperatures above their melting point. At temperatures >1100 ˚C the CMAS attack mechanisms may be characterized as thermo-mechanical and thermo-chemical. The thermo-chemical attack results in dissolution of the desired tetragonal metastable *t*' phase due to depletion of Y_2O_3 and re-precipitation of destabilized ZrO_2 and Zr-bearing particles depending on the local chemistry of the CMAS melt [8, 11]. The thermo-mechanical attack is due to the infiltration of the CMAS melt into the inter-columnar gaps of the TBC influenced by capillary forces. The depth of CMAS infiltration is controlled by fluid properties such as viscosity and surface tension as well as the microstructure of the TBC [12]. As the melt flows down into the TBC it solidifies, thereby filling its porous features generating a stiffening of the coating which leads to loss of strain tolerance and delamination of the TBC [13-15]. For the case of initially glassy particles such as many volcanic ashes, the thermo-mechanical attack can be incipient at temperatures far below the thermodynamic melting temperature. Softening and flow of molten ash just above the glass transition temperature are the prevailing mechanisms here [16-18].

Several efforts have been made to understand the characteristics of CMAS attack and to generate mitigation techniques based on novel TBCs that are resistant to CMAS infiltration [4]. The most studied CMAS mitigation approach is based on the use of a reactive coating that induces crystallization of the melt, thereby generating stable crystalline reaction products which seal the TBC pores and thus prevent further infiltration [19-26]. Additionally, promising results have been obtained in reducing the CMAS infiltration by tuning the TBC microstructure [12]. That study relied on the modification of the microstructural features of the 7YSZ TBC, specifically the shape and distribution of the nanometer-scale secondary columns present at the edges of the columns - so-called "feather-arms". The feather-arms are believed to act as open channels that distribute the melt due to a microstructural tortuosity which lengthens the infiltration path and/or changes the capillary pressures, thereby impeding deeper infiltration. In order to model the infiltration behavior of CMAS, experimental data for the high temperature viscosity, surface tension and the contact angles are required - all properties that depend strongly on the chemical composition of the melt. Wiesner et. al. [27] have used different viscosity models to estimate the viscosity of a CMAS melt and observed discrepant results between those models. To obtain reliable estimates of the viscosity of the CMAS melts investigated here we have experimentally determined the viscosity. Along with porosity and contact angle determinations, those values are embedded in the infiltration model presented here.

This study proposes a novel approach to predict CMAS melt infiltration into EB-PVD TBCs which is based on a physical model considering two different approaches for coating permeability ('concentric pipe' vs. 'open pipe'). A similar approach to the open pipe model has been proposed before in literature [28] but there the fluid is considered to fully wet the TBC surface (Contact angle = 0). Finally, we compare the concentric and open pipe infiltration approaches with experimental measurements performed at short term infiltration (30 sec to 8 min) in standard 7YSZ coatings at 1250˚C.

2. Experimental Procedures

2.1 Sample processing

Standard 7YSZ coatings were deposited using a 150 kW EB-PVD system on a single evaporation source matching the standard 7YSZ composition. Coatings were deposited with a thickness of 400 to 420 µm on 1 mm thick alumina plates. The high thickness was selected to enable the identification of an effective infiltration depth without reaching the alumina substrate too early. Two microstructures - "normal" and "feathery" - were deposited by varying deposition temperature and rotation of the sample holder as described in a previous study [12]. The summary of microstructural features such as porosity, column/diameter, and inter-columnar gap width is given in **Table 1.** The porosity values shown were obtained by the helium pycnometry method and the column and inter-columnar gap width represent the average of the values specified previously (see Table 2 in [12]).

2.2 Infiltration and characterization

CMAS melt infiltration experiments were carried out using two synthesized CMAS sources identified as CMAS 1 and CMAS 2. Their preparation parameters are specified in a previous publication [6]. The chemical composition and melt properties are presented in **Table 2** as obtained previously from DSC measurements [6]. The thermal tests were performed by deposition of CMAS powder on top of the coatings at 20 mg/cm^2 of concentration. Next, heat treatments were performed using a cyclic furnace for short-term infiltration intervals varying from 30 s to 8 min. at 1250°C. The samples were moved into the hot furnace and heated to 1250°C within 8 min. (± 15 s), followed by isothermal heating of the coatings for the specified ranges from 30 s to 8 min. and finalizing with air quenching (18 K/s cooling rate) to room temperature. The heating profile is specified in **Fig. 1** which was obtained by specifically attaching a thermocouple on the top surface of the sample to monitor its temperature. The heat ramping is considered until the moment when the temperature reaches 1250°C (at about 8 min.). The temperature variation during the isothermal heating was carefully controlled by specifically calibrated thermocouples that allow a maximum temperature deviation of 5 K. Lastly, the generated peak in the temperature curve after 200 s in **Fig. 1** was a result of ramp rate adjustment by the controller to approach the set temperature.

Standard metallographic techniques were used for cross-sectional imaging. The CMAS infiltration depth was determined by using an SEM (DSM Ultra 55, Carl Zeiss NTS, Wetzlar, Germany) equipped with an EDS system (Inca, Oxford Instruments, Abingdon, UK). High magnification imaging combined with Si elemental mapping and spot analysis helped to identify the maximum infiltration depth.

2.3 Viscosity and contact angle measurement

The viscosity-temperature relationships of both CMAS 1 and CMAS 2 melts were measured in air, at 1 atm. in the temperature range between 1000-1350°C with a Brookfield RVTD viscometer head. A $Pt_{80}Rh_{20}$-spindle and crucible were used with a cross section of 45° conical ends and 0.14 diameter. The viscosimeter head and spindle were calibrated for viscosity

determinations using “Deutsche Glastechnische Gesellschaft - “DGG1” standard calcium-sodium silicate glass. The accuracy of determination is taken as the sum of uncertainties from standard and sample determinations at ± 6% (2sigma). CMAS mixtures of 70 grams were pulverized with alcohol in an agate mortar for 3 h and then decarbonated at 800°C overnight. These powders were fused at 1350°C for 3 h in a 25 cm^3 Pt crucible. Prior to viscosity measurements, fused samples were poured from the Pt crucible into the crucible used for the viscosity determinations and stirred with the spindle for 1h at 1350°C resulting in a homogeneous, bubble-free melt. The viscosities were measured with More information about this method is available in the literature [29].

The high temperature contact angle measurements of the molten CMAS droplets were performed by monitoring the morphological changes in a heating microscope (EM301 Hesse instruments). The CMAS powder was pressed with a stress of 1.5 $N.mm^{-2}$ into a cylindrically-shaped pellet (3 mm diameter by 3 mm height, according to CEN/TS 15443 procedures) and then heated up to 1400°C at a rate of 10°C/min in air at ambient pressure on alumina substrates, as described in the literature [17, 18]. The mean contact angle was evaluated from the left and right side of the samples

In addition, the contact angle measurements were repeated on top of as coated TBCs without any surface treatment. The coatings were deposited on alumina substrates as explained in section 2.1. The changes in the height, area and contact angle of the pressed compounds with respect to temperature were monitored at 1 Hz sampling rate by a charge-coupled device (CCD) camera, which captured 2D cross-sectional silhouette images of the cylinder. Special attention has been put to record the change in contact angle which was measured with the help of an imaging software package included with the heating microscope. The recorded contact angle is specified in **Fig. 3**. Additionally, depending on the shape of the CMAS cylinder, the shape evolution can be parameterized via characteristic temperatures such as deformation temperature and hemisphere temperature (DT and HT respectively). Those temperatures are described in detail in previous studies for volcanic ash melting behaviors such as the ability for ashes to stick to surfaces due to melting (DT) and to spread and wet surfaces (HT) [17, 18]. The heating microscope was calibrated with a gold sample which gave a temperature shift of +10 degrees (1074° instead of 1064°).

2.4 Specific surface area and porosity measurement

Measurements for specific surface area and porosity were performed on coatings deposited on alumina substrates. The influence of the substrate was considered and where necessary the raw data was related to the actual coating volume and weight. Nevertheless, all internal surfaces of the coating were available for measurements due to the open nature of the porosity present. The specific surface area of the 7YSZ samples was measured by nitrogen physisorption at liquid nitrogen temperature of 77 K. The device TriStar II 3020 from Micromeritics was chosen for this purpose. Approximately 0.15 grams of a coated sample with the alumina substrate was weighed into a glass sample tube which was then set under vacuum below 0.1 mbar and a temperature of 120°C. After 3 h of pretreatment, measurements were conducted recording 88 data points from 0 to 1 relative pressure of 6.0 pure nitrogen gas. The specific surface area was calculated from

measurement data utilizing the BET (Brunauer-Emmett-Teller) equations. The same set of hysteresis data was analyzed with BJH (Barrett-Joyner-Halenda) equations. The resulting pore size distribution gave information on the mesopore area from 2 to 50 nm. Further information on the procedure of nitrogen physisorption measurements can be obtained from the literature [30].

The skeletal density was measured by Helium pycnometry at room temperature. The device AccuPyc 1340 from Micromeritics with Helium of 6.0 purity was used for this purpose. Ten measurements were performed of which a mean value is reported. The enveloped density was calculated from geometric dimensions of the coatings which were measured in [mm] (and converted into volume v) with a mechanical caliper of two decimal places. Porosity was calculated from enveloped density and skeletal density following equation (1) where ρ_e is the enveloped density and ρ_s is the skeletal density. Closed pores are not available to helium pycnometry measurements. If present, closed pores decrease the skeletal density.

$$P = \left(1 - {}^{\rho_e}/_{\rho_s}\right) * 100 \ \ v/v \ \% \tag{1}$$

3. Results

3.1 Viscosity and contact angle of CMAS melts

The measured viscosities for the CMAS melts are plotted in **Fig. 2** as a function of temperature. CMAS 2 exhibits a lower viscosity than CMAS 1. At 1250°C CMAS 2 exhibits 4.0 Pa.s while CMAS 1 6.9 Pa.s. The plot also shows a significant difference between the experimental viscosities and calculated values using the model proposed by Giordano et al. [31] (GRD) which predicts viscosity from major oxides present in the silicate melts. The contact angle images from the heating microscope at temperatures ranging from 1243 to 1266°C are shown for alumina substrates in **Fig. 3**. The initial shape of the CMAS 1 cylinder shown in **Fig. 3a** is partially lost at 1250°C which could be attributed to the partial softening of the compound. The temperature at which the shape of the cylinder is lost due to softening is called 'deformation temperature (DT)' as reported in previous studies for the melting behavior of volcanic ashes [17, 18]. The right angle cylindrical shape is fully lost at 1260°C generating a 58° contact angle with respect to the surface. Then, the angle decreases to 43° within a range of a 6 K increase in temperature which is consistent with full softening and wetting of the sample to an equilibrium geometry controlled by the surface forces. CMAS 2 (**Fig. 3b**) reaches DT at 1243°C (7 Kelvin less than CMAS 1). This could translate to enhanced physical infiltration dynamics with respect to CMAS 1. The right angle cylindrical shape is fully lost by 1248˚C yielding a 57˚ contact angle. Again, the contact angle reduces at 1250˚C within two Kelvin increase down to 44˚. The larger variation in contact angle for CMAS 2 confirms its lower viscosity and a higher infiltration potential.

3.2 Porosity of TBCs, specific surface area and pore size distribution

The porosity results obtained from the helium pycnometry measurements relate only to the open accessible pores and are presented in **Table 1** for each microstructure. The overall porosity of the 'normal' microstructure is 14.5 v/v % whereas the porosity of the 'feathery' microstructure was measured to be twice as high at 29.5 v/v %. The 'feathery' microstructure exhibits a higher porosity due to the larger presence of intra-columnar feather arms. Additionally, it shows a larger

number of inter-columnar gaps available compared to the ‘normal’ microstructure as specified previously [12].

Nitrogen adsorption isotherms used for BET calculations are plotted in **Fig 4a**. The specific surface area of the TBCs for ‘normal’ was recorded as 1.4 m^2/g and 5.7 m^2/g for the ‘feathery’ samples. A comparative graph for the specific surface area (SSA) is provided in **Fig.4b**. Correspondingly, the obtained SSA values are consistent with the results obtained in previous studies with different TBC morphologies generated by varying coating parameters using EB-PVD [32]. The lower deposition pressure used in this study ($6x10^{-3}$ mbar) provides a lower SSA than the coatings produced at higher pressure ($8x10^{-3}$ mbar) previously.

Pore size distributions obtained from the BJH analysis are plotted in **Fig 4c**. The mesopore size distribution of ‘feathery’ in comparison to ‘normal’ coatings is significantly shifted to smaller diameters. In addition to that the total mesoporous volume of the ‘feathery’ coatings is more than twice than that of the ‘normal’ coatings, see **Fig 4d**. Mesopores of 25 and 8 nm diameters are much more present in the case of ‘feathery’ coatings. The pronounced peak for the ‘feathery’ sample at 4 nm was recorded repeatedly and confirmed with several measurements on the same sample. It is likely that the peak appearance at 4 nm is due to narrow tubular channels at the end of each feather arm.

3.3 Infiltration depth profiles

The short term infiltration experiments were performed to effectively investigate the influence of different microstructures on the CMAS infiltration kinetics. Furthermore, the infiltration experiments are used as a base for the validity of the calculated infiltration depth generated from the models. **Fig. 5** shows a cross-sectional SEM image (A) for the ‘normal’ microstructure under CMAS 1 infiltration after 30 s and its respective Si elemental mapping (B) showing the infiltration zone delimited within the dotted lines. It can be seen that 7YSZ offers no resistance to CMAS infiltration and CMAS has penetrated 155 µm deep into the ‘normal’ microstructure after only 30 s of infiltration time. In addition, both microstructures did not show any degradation or re-precipitation of reaction products, meaning that no reactive crystallization took place during the very short testing times (2, 5 and 8 min.). This ensures that the infiltration is not influenced by chemical reaction and no time delay in infiltration is generated thereby. The infiltration results of ‘normal’ and ‘feathery’ microstructures are shown in **Fig. 6** for CMAS 1 and only for the feathery microstructure infiltrated with CMAS 2 after 2 min. The measurements were performed by using EDS mapping and spot analysis to trace for Si and Ca in 5 different infiltrated areas per sample. The error bars represent the standard deviation from the imaging measurements. The results show slower infiltration kinetics in the ‘feathery’ microstructure compared to ‘normal’. This effect was observed for both CMAS compositions (with different melt viscosities). In the case of CMAS 1, the infiltration depth was reduced up to 44 %, and 24 % for CMAS 2. Another important observation is the deeper infiltration of CMAS 2 (320 µm) after 2 min. in the ‘feathery’ microstructure which represents more than twice the infiltration of its counterpart CMAS 1 (125 µm) under the same testing conditions. The infiltration plot for CMAS 1 in **Fig. 6** shows a nearly linear infiltration trend with time for both microstructures.

This could not be determined for CMAS 2 since only 2 data points until 2 min. were available due to complete infiltration at that time.

4. Discussion

From the results, it has been demonstrated that the 'feathery' microstructure reduces the infiltration kinetics compared to the 'normal' structure under the same testing conditions for CMAS 1 and CMAS 2, in accordance with previous results reported for CMAS 1 at a lower temperature [12]. Those experiments were performed at 1225°C and the 'feathery' structure was found to be 200% more effective in reducing the infiltration depth compared to the normal 'microstructure' after 20 h. At 1250°C, this effect has been reduced to 44% for the CMAS 1 melt. The ratio of measured overall porosities for 'feathery' to 'normal' is almost 2:1 and it is expected that a highly porous material would be infiltrated faster. In contrary, for both CMAS compositions, the 'feathery' structure offered better resistance. This surprising behavior may be explained on the basis of how pores are interconnected in both microstructures. The 'normal' structure exhibits a more uniform microstructure, with respect to the distribution of columns and smaller feather arms throughout its thickness as compared to 'feathery' as reported previously [12]. Thus, the path of the melt is not distributed as effectively for the 'normal' as for the 'feathery' structure. Additionally, as can be seen from **Fig. 4b,** the specific surface area for pores in the 'feathery' structure is 4 times higher than in 'normal' structure. The larger SSA of the 'feathery' can be explained from the combination of narrower and more porous columns (i.e. more feather arms) with more available inter-columnar gaps. Moreover, the mesopore volume for 'feathery' structure is more than twice that of the 'normal' structure, which could mean that more voids between feather arms are available for the 'feathery' microstructure to delay the CMAS flow through the columnar gap. It is believed that this pore network which acts as a series of capillary tubes which lie at an angle to the principal infiltration direction reduces the capillary pressure in the intercolumnar gaps. The expediency of EB-PVD process allows tailoring of the TBC microstructure in such a way that both macro and mesopore structure can be altered to accomplish the desired properties as shown in **Fig. 4**. A pervasive study on the variation of EB-PVD morphology and its pursuance on the thermal conductivity was studied in detail [33]. An analogous approach can be considered to study the fundamental aspects of EB-PVD microstructural effects on the CMAS infiltration kinetics.

A 24% effect in the case of CMAS 2 suggests the fact that for the melts with low viscosities or at very high temperatures the microstructure role becomes insubstantial. i.e., if the infiltration temperatures are chosen beyond 1270°C, the microstructural effects can be negligible for CMAS compositions as the infiltration proceeds in a few seconds. However, for volcanic ash compositions, this effect still can be substantial as their viscosities lie in the range of 1-2 orders of magnitude higher with respect to CMAS compositions [18, 31, 34]. Furthermore, when a reactive TBC material which promotes the crystallization of the CMAS melt is considered, the optimization of its microstructure would give an additional sufferance in inhibiting the CMAS infiltration. Previous results using 65 wt.% Y_2O_3- 35 wt. % ZrO_2 coatings under the same testing conditions for 5 min. have shown a CMAS 1 infiltration of 38 µm [35]. This represents a significant improvement in infiltration resistance compared to the 400 µm infiltration for

‘normal’ microstructure and 230 for ‘feathery’ under CMAS 1 infiltration. In addition, the microstructure of these CMAS resistant coatings was not specifically tailored to target an enhanced infiltration resistance, thus, it was believed that a higher infiltration resistance could be achieved by means of microstructure tuning.

The microstructural parameter ‘tortuosity’ has been proposed in the literature [8, 12, 27, 28] as one of the main parameters controlling the melt infiltration. Tortuosity represents a ratio factor that accommodates the resistance to flow for a certain fluid that travels in a non-vertical path due to the arrangement of the capillaries available. However, some EB-PVD microstructures are tailored in such a way that TBC columns are fairly parallel with almost straight paths of columnar gaps meaning that this ‘tortuosity’ definition seems to be trivial. Consequently, tortuosity is conceived as a ‘geometric factor’ which considers the ratio of available area for infiltration due to the feather arm distribution with respect to a columnar gap area from point A to point B as seen in **Fig. 7a**. By tuning the TBC microstructure, the ‘geometric factor’ can be optimized in such a way that a significant improvement in infiltration resistance can be achieved. Since the ‘normal’ microstructure exhibits wider inter-columnar gaps and less open voids between feather arms compared to the ‘feathery’ (see Fig. 10 in [12]), its geometric factor is smaller. Further information on the geometric factor is given in section 4.1 for each microstructure.

Another important and yet to be understood factor on the infiltration is the change in the contact angle of the CMAS liquid at the longer feather arms which obstructs the flow into them generating an effect of nano-spike interaction with the fluid as shown in **Fig. 7b**. In the studied temperature regime up to 1266°C, heating microscope experiments have revealed that CMAS melts do not completely wet the surfaces and the contact angles are not close to zero (max 42°). It is known from the literature that modifying coating surfaces can lead to different wetting and flow behaviors [36, 37]. The combined effects of the geometric factor and the liquid behavior on nano-surfaces should provide a more accurate shape factor which will eventually need to be extracted from different microstructures. That general goal is, however, beyond the scope of this paper.

The basis of the physical model used to predict CMAS infiltration in this study was proposed by Zhao et al. [28] and modified later [12] by deriving Darcy’s law for the steady-state uni-directional flow of viscous liquids through a porous medium. The final equation (2) predicts an infiltration time *t* for a given infiltration depth *h* and a radius *r* open for infiltration, which is as follows:

$$t = \frac{\mu r h^2}{2\sigma k \cos\theta} \qquad (2)$$

Where the factors μ, σ and θ represent fluid properties (viscosity, surface tension and contact angle respectively), *r* and *k* are controlled by the TBC microstructure (radius open for infiltration and permeability respectively). The permeability of the infiltrated medium (*k*) represents the main parameter that governs infiltration. In practice, it can be controlled via microstructure refining. Two different definitions are used in this paper to evaluate the permeability which are called ‘open pipe’ and ‘concentric pipe’ as described previously [12].

i) The ‘open pipe model’ considers the columnar gap as a single capillary tube/pipe that is open for infiltration as seen in **Fig. 8a,** the permeability equation (3) for the open pipe model (k_o) is then as follows:

$$k_o = \frac{r^2\varphi^2}{8\tau(1-\varphi)^2} \quad (3)$$

Where r still represents the radius of the columnar gap (**Fig. 8c**) open for infiltration, φ represents the coating pore fraction (see Table 1) and τ is the geometric factor of the coating expressed as the ratio of the overall area of the columnar gap with respect to the overall area of total number of feather arms available in the coating.

ii) The ‘concentric pipe model’ considers the TBC column and the columnar gap as a pipe with a kernel located concentrically inside as seen in **Fig. 8b. T**he radius of the column (kernel ‘a’) and columnar gap (open area for infiltration ‘b’) are considered together as seen in **Fig. 8d**. The equation (4) is as follows:

$$k_c = \frac{\varphi}{8\tau^2} b^2 \left[1 + \frac{a^2}{b^2} + \left(1 - \frac{a^2}{b^2}\right) . \frac{1}{\ln\frac{a}{b}}\right] \quad (4)$$

By substituting equation (3) and equation (4) for each model into equation (2) the final infiltration time equation is obtained for each model. However, in the case for the concentric pipe model, only the radius r specified in the equation (2) becomes the following new radius (r_c) described in the equation (5):

$$r_c = \sqrt{b^2 - a^2} \quad (5)$$

Where ***a*** and b are still the values specified in **Fig. 8d**.

Contrary to previous approaches [8, 19, 27, 38], the measured experimental values of viscosity, contact angle, porosity, geometric factor, and surface area were used to calculate the infiltration depths using both the concentric and open pipe models. The surface tension was estimated using the equation for silicate glasses at 1400˚C proposed by Kucuk et al. [39] (**Table 3**). The surface tension is assumed to not vary significantly from 1200 to 1500˚C [8, 27].

4.1 Infiltration prediction for CMAS 1

The infiltration depth predictions for CMAS 1 and CMAS 2 are summarized in **Tables 4** and **5**, respectively. The results compare the prediction of the physical models (open pipe, concentric pipe) with the infiltration experiments at 1250˚C tested for 2 min. for both microstructures. Consecutively, the values show the calculations using the measured contact angle at 1250°C for each CMAS compound as seen in **Fig. 3**. The data shown in **Table 4** indicate an approximately 3.5 times higher infiltration depth prediction when the GRD viscosity is used instead of experimental viscosity by all used models for CMAS 1. It is important to note that the predicted value from the GRD model provides about 12 and 20 times lower viscosities for CMAS 1 and 2, respectively, when compared with the experimentally measured values. Similarly, a significant variation in predicted viscosities for a CMAS compound using different methods (including GRD) has been reported in the literature [27]. This discrepancy in our results is likely from the

calibration of GRD in 10 component natural volcanic melt compositions where it works quite well but which is challenged when extended to synthetic CMAS melts of fewer components (especially SiO_2 below 41 wt. %) than the calibration region [31]. This incongruity creates the incumbency to use the experimentally determined viscosity values to provide accurate estimations. Furthermore, the calculations show that the concentric pipe model predicts the infiltration depth of 170 µm and 95 µm for 'normal' and 'feathery' microstructures respectively. This represents an error of 29 percent for 'normal' microstructure and 24 percent for 'feathery' with respect to the experimentally determined depths of 240 and 125 µm. From the testing conditions, one can infer that two main factors are influencing the kinetics of infiltration for the CMAS compositions which cannot be estimated exactly and can lead to deviation from the experimentally measured values.

i) The variation of the contact angle with different microstructures. This can influence the wetting interaction of the fluid with both, the coating surface and the feather arms. Henceforth, an additional study of the contact angle for CMAS 1 only was performed on the normal and feathery TBC surfaces using the same heating microscope procedure as described in section 2.3. The results of this experiment are shown in **Fig. 9a** and **b** for normal and feathery structures respectively at different temperatures. It is noted that the contact angle and melting of the CMAS 1 compound behaves differently for each microstructure. The finer 'feathery' microstructure (see **Table 1** and reference [12]) generates a higher contact angle than the 'normal' structure at the TBC top surface (e.g. 52° at 1266 °C compared to 35° at the same temperature). Therefore, it seems that the lower wetting generated on the feathery microstructure promotes its higher infiltration resistance in addition to the longer feather arms. It seems that the deformation temperature (DT) is reached for the heating microscope samples (**Figs. 3a** and **9**) within the range of 1260-1264˚C which correlates with the melting temperature obtained from the DSC experiments (between 1258-1265°C for ref. [6]). This could lead to the conclusion that the melting response appears to be an intrinsic characteristic of the compound and it is not controlled by the furnace. Complementary heating microscope experiments will be performed by keeping the temperature constant at 1250˚C to see the variation of the contact angle with respect to testing time. In addition, it has been demonstrated that the microstructure of EB-PVD Gadolinium Zirconate exhibits a strong influence on the CMAS resistance [40], reducing CMAS infiltration by 50 percent on coatings exhibiting a combination of fine columns and narrow inter-columnar gaps. Clearly, the combination of an efficient microstructure architecture with a reactive material holds the potential for even greater CMAS mitigation.

The wetting behavior of the fluid interacting with the nano-features inside the inter-columnar gaps such as feather arms' tips is expected to vary as well for each microstructure generating a wetting or non-wetting behavior which restricts or promotes the flow into the feather arms as seen in **Fig. 8b**. However, to the knowledge of the authors, it is unpractical to measure this wetting effect at such small scale inside a coating and at high temperatures (above 1250 °C). For this reason, the predicted depth values from Tables **4** and **5** consider a fixed contact angle at 1250°C obtained from the initial measurements on top of the alumina surface given in **Fig. 3** (67° and 43° for 'normal' and 'feathery'). Furthermore, the infiltration depth with respect to contact angle for each model is plotted in **Fig. 10a** for CMAS 1. The plot shown exhibits a

significant variation of infiltration depth as a function of contact angle. The blue dotted line represents the contact angle recorded at 1250 °C (67 degrees) for the CMAS 1 composition. The difference in predicted infiltration depth comparing zero degree contact angle with 67° in the concentric pipe model is about 102 μm for 'normal' and 56 μm for 'feathery' microstructures. These results show that the assumption of full wetting can lead to the overestimation in infiltration depth prediction and actual measured angles on top of the material lead to underestimation. Furthermore, it is seen from the graph that the measured contact angles for the TBC (**Fig. 9**) microstructures provide a larger underestimation of infiltration.

ii) The variation of TBC column width and feather arm dimensions with respect to the coating depth of the TBC [12] affects the rate of infiltration (change in geometric factor). For instance, it is highly difficult to precisely estimate the change in geometric factor with respect to depth which has limited this study to use an overall estimated parameter for the first 100 μm of coating depth where the pore and column distribution is more uniform.

The τ value referred as tortuosity is reported in the range of 1 to 3 in the literature [8, 27, 28, 41]. It is believed that the geometric factor (τ) for this study has to represent a larger factor for the feathery microstructure than for the normal. This is due to the larger amount of feather arms present in the feathery TBC. Consequently, the factors were estimated by the use of imaging software (image J) at two different sites. The measured values below represent the average of 2 measurements where the area of the TBC columnar gap was compared to the open area for infiltration of the feather arms as seen from **Fig. 11**. The columnar gap (CG) area was assumed to be constant throughout the thickness of the coating for 'normal' and 'feathery' (a and b respectively in **Fig. 11**) at an average of 3.4 (±0.3) and 3.3 (±0.6) μm^2 respectively. Then the average feather arm area was also assumed constant through the coating thickness and was measured for 'normal' and 'feathery' with values of 2.7 (±0.5) and 7.5 μm^2 (±0.9). The fitting geometric factor parameters derived from those values for 'normal' and 'feathery' microstructures are 1.25 and 2.31 respectively which fall within the reported values from the literature. They were calculated as the quotient between the columnar gap area and average feather arm area. It is important to note that the highest estimated value represents the numerator (columnar gap area for 'normal' and feather arm area for 'feathery') since it represents the area that will retain the higher fluid quantity. **Fig. 10b** compares the predicted infiltration depth vs. the experimentally measured values with respect to time in the case of CMAS 1 feathery sample. It is seen how after 5 min the open pipe model starts to get closer to the experimental measurement compared to the concentric approach. After 8 min both models provide an underestimation in infiltration prediction but still the open pipe provides the closest prediction (353 μm). This time dependent variation is believed to be due to the geometric factor effect since at higher depths the geometric factor should become smaller which means that a higher infiltration rate is expected.

4.2 Infiltration prediction for CMAS 2

The predicted results for CMAS 2 are presented in **Table 5** where the closest agreement between experiment and prediction is given by the concentric pipe model. Additionally, the results in **Table 5** exhibit as well a larger prediction in infiltration depth about 4.5 times more for the GRD

viscosity. The difference between the predicted value for ‘feathery’ (286 µm) with respect to the infiltration experiment (320 µm) is about 11 percent. The predicted infiltration for ‘normal’ microstructure could not be compared with the experimental result since the coating was fully infiltrated after the experiment. However, the concentric pipe model predicts an infiltration depth of 515 µm which is reasonable but it could not be experimentally proven. Moreover, it is important to note that the infiltration time considered for this test is 330 seconds. Since the partial melting of the CMAS 2 compound starts at about 1243°C which represents the DT temperature where the contact angle is 67 degrees as seen in **Fig. 3b**. Thus, the real testing time adds the 210 seconds that the system takes to heat up from 1243 to 1250°C as seen from the furnace’s heating profile given in **Fig. 1**. Although the viscosity and contact angle vary during the 210 required for specified temperature rise, the values used for the predictions in **Table 5** were fixed at 1250°C (4.0 Pa.s and 44° respectively) to simplify the prediction.

The difference in the predicted infiltration depth comparing zero degrees contact angle with 44° in the concentric pipe model is about 87 µm for ‘normal’ and 49 µm for ‘feathery’. Once again it is obvious that full wetting can lead to the overestimation in infiltration depth prediction and actually measured angles on top of an alumina substrate lead to underestimation.

The current results indicate that the proposed approach of a concentric pipe provides a more realistic approximation as seen from this study of the EB-PVD microstructure. However, the uncertainty in measuring the contact angles very precisely as a function of temperature and more realistically also inside the TBC inter-columnar gaps, and determining the correct shape factors are the main impediments in calculating the infiltration depths more accurately. Nevertheless, the CMAS related research has been reached a state, where models using thermodynamic equilibrium calculations coupled with infiltration kinetics are developed which come closer to the actual scenario in an engine [41, 42]. Over/underestimating the infiltration depth would lead to large errors in predicting the lifetime of a TBC coating under CMAS attack. Hence, the proposed concentric pipe model appears to be more reliable and explicit in predicting the infiltration kinetics. Future studies will be performed to optimize the results for transient conditions with changes in viscosity and contact angles over infiltration time and thermal gradients.

5. Conclusions

Standard 7YSZ TBCs deposited by EB-PVD with two different microstructures, namely ‘normal’ and ‘feathery’, were tested for CMAS infiltration at short-term heat treatment (30 s to 8 min.). The measured infiltration results were compared with calculated infiltration data from a physical model previously proposed with two different permeabilities (‘concentric’ and ‘open’ pipe) and a previous infiltration model used in literature. The viscosity and contact angle of the tested CMAS melts were experimentally determined and their measured values were considered for the mathematical infiltration prediction. The TBC porosity was also measured experimentally and used for infiltration prediction. The following conclusions were generated from the results:

- Short time infiltration experiments under well-controlled conditions represent a powerful tool to understand, differentiate and effectively predict the infiltration kinetics in EB-PBD TBCs with different microstructures. The 'Feathery' microstructure shows better CMAS resistance compared to its 'Normal' counterpart.
- A significant correlation between coating microstructure and the wetting behavior of CMAS was found. The finer EB-PVD columns offer more resistance to the CMAS wetting by increasing the contact angle towards higher numbers and combining more feather arms to split the glass flow.
- The experimental viscosity values are found to be one order of magnitude higher compared to the Giordano-Russell-Dingwell (DRD) model values.
- The comparison of calculated and experimental data reveals that the 'concentric pipe model' provides a more realistic approach for predicting CMAS infiltration into EB-PVD TBCs than the 'open pipe model'. However, limitations are present due to the discrepancy in the contact angle in interaction with different surfaces. In addition, the microstructural effect i.e. geometric factor changes with TBC thickness which could not be considered so far.
- The physical concentric pipe model could serve as a baseline for optimization and development of new microstructures that can delay CMAS infiltration. The more complex approaches will consider more realistic environments under temperature gradients, microstructure variations and interaction with new CMAS resistant materials.
- For accurate calculation of the infiltration behavior, precise measurements for all relevant parameters such as viscosity, surface tension, contact angle, and permeability is mandatory.

Acknowledgment

The authors would like to thank S. Kolzenburg for assistance in viscosity data reduction. The authors also thank D. Peters, A. Handwerk and J. Brien for their technical assistance during TBC preparation and testing. The authors thank the Deutsche Forschungsgesellschaft (DFG) for funding this project (project no. SCHU 1372/5-1).

6. References

1. Borom, M.P., C.A. Johnson, and L.A. Peluso, *Role of environment deposits and operating surface temperature in spallation of air plasma sprayed thermal barrier coatings.* Surface and Coatings Technology, 1996. **86**: p. 116-126.
2. Braue, W., P. Mechnich, and D.J. Green, *Recession of an EB-PVDYSZ Coated Turbine Blade by $CaSO_4$ and Fe, Ti-Rich CMAS-Type Deposits.* Journal of the American Ceramic Society, 2011. **94**(12): p. 4483-4489.
3. Clarke, D.R., M. Oechsner, and N.P. Padture, *Thermal-barrier coatings for more efficient gas-turbine engines.* MRS bulletin, 2012. **37**(10): p. 891-898.
4. Levi, C.G., et al., *Environmental degradation of thermal-barrier coatings by molten deposits.* MRS Bulletin, 2012. **37**: p. 932-941.
5. Mechnich, P., W. Braue, and U. Schulz, *High-temperature corrosion of EB-PVD yttria partially stabilized zirconia thermal barrier coatings with an artificial volcanic ash overlay.* Journal of the American Ceramic Society, 2011. **94**(3): p. 925-931.

6. Naraparaju, R., et al., *Degradation study of 7wt.% yttria stabilised zirconia (7YSZ) thermal barrier coatings on aero-engine combustion chamber parts due to infiltration by different CaO-MgO-Al_2O_3-SiO_2 variants.* Surface and Coatings Technology, 2014. **260**: p. 73-81.
7. Naraparaju, R., et al., *The Accelerating Effect of $CaSO_4$ Within CMAS (CaO-MgO-Al_2O_3-SiO_2) and Its Effect on the Infiltration Behavior in EB-PVD 7YSZ.* Journal of the American Ceramic Society Ceramic Society, 2016. **99**(4): p. 1398-1403.
8. Krämer, S., et al., *Thermochemical interaction of thermal barrier coatings with molten CaO–MgO–Al_2O_3–SiO_2 (CMAS) deposits.* Journal of the American Ceramic Society, 2006. **89**(10): p. 3167-3175.
9. Nicholls, J.R., et al. *Low thermal conductivity EB-PVD thermal barrier coatings*. in *Materials science forum*. 2001. Trans Tech Publ.
10. Nicholls, J.R., et al., *Methods to reduce the thermal conductivity of EB-PVD TBCs.* Surface and Coatings Technology, 2002. **151-152**: p. 383-391.
11. Pujol, G., et al., *Step-by-step investigation of degradation mechanisms induced by CMAS attack on YSZ materials for TBC applications.* Surface and Coatings Technology, 2013. **237**: p. 71-78.
12. Naraparaju, R., et al., *Tailoring the EB-PVD columnar microstructure to mitigate the infiltration of CMAS in 7YSZ thermal barrier coatings.* Journal of the European Ceramic Society, 2017. **37**(1): p. 261-270.
13. Chen, X., *Calcium-magnesium-alumina-silicate (CMAS) delamination mechanisms in EB-PVD thermal barrier coatings.* Surface and Coatings Technology, 2006. **200**: p. 3418-3427.
14. Mercer, C., et al., *A delamination mechanism for thermal barrier coatings subject to calcium–magnesium–alumino-silicate (CMAS) infiltration.* Acta Materialia, 2005. **53**(4): p. 1029-1039.
15. Evans, A.G. and J.W. Hutchinson, *The mechanics of coating delamination in thermal gradients.* Surface and Coatings Technology, 2007. **201**: p. 7905-7916.
16. Kueppers, U., et al., *The thermal stability of Eyjafjallajökull ash versus turbine ingestion test sands.* Journal of Applied Volcanology, 2014. **3**(1): p. 4.
17. Song, W., et al., *Fusion characteristics of volcanic ash relevant to aviation hazards.* Geophysical Research Letters, 2014. **41**(7): p. 2326-2333.
18. Song, W., et al., *Volcanic ash melting under conditions relevant to ash turbine interactions.* Nature communications, 2016. **7**.
19. Aygun, A., et al., *Novel thermal barrier coatings that are resistant to high-temperature attack by glassy deposits.* Acta Materialia, 2007. **55**: p. 6734-6745.
20. Eils, N.K., P. Mechnich, and W. Braue, *Effect of CMAS Deposits on MOCVD Coatings in the System Y_2O_3–ZrO_2: Phase Relationships.* Journal of the American Ceramic Society, 2013. **96**(10): p. 3333-3340.
21. Drexler, J.M., et al., *Jet engine coatings for resisting volcanic ash damage.* Advanced Materials, 2011. **23**(21): p. 2419-2424.
22. Krause, A.R., et al., *2ZrO2·Y2O3Thermal Barrier Coatings Resistant to Degradation by Molten CMAS: Part I, Optical Basicity Considerations and Processing.* Journal of the American Ceramic Society, 2014. **97**(12): p. 3943-3949.
23. Krause, A.R., et al., *2ZrO2·Y2O3Thermal Barrier Coatings Resistant to Degradation by Molten CMAS: Part II, Interactions with Sand and Fly Ash.* Journal of the American Ceramic Society, 2014. **97**(12): p. 3950-3957.
24. Schulz, U. and W. Braue, *Degradation of La2Zr2O7 and other novel EB-PVD thermal barrier coatings by CMAS (CaO-MgO-Al2O3-SiO2) and volcanic ash deposits.* Surface and Coatings Technology, 2013. **235**: p. 165-173.

25. Krämer, S., J. Yang, and C.G. Levi, *Infiltration-Inhibiting Reaction of Gadolinium Zirconate Thermal Barrier Coatings with CMAS Melts.* Journal of the American Ceramic Society, 2008. **91**(2): p. 576-583.
26. Mechnich, P., W. Braue, and D.J. Green, *Volcanic Ash-Induced Decomposition of EB-PVD $Gd_2Zr_2O_7$Thermal Barrier Coatings to Gd-Oxyapatite, Zircon, and Gd,Fe-Zirconolite.* Journal of the American Ceramic Society, 2013. **96**(6): p. 1958-1965.
27. Wiesner, V.L. and N.P. Bansal, *Mechanical and thermal properties of calcium–magnesium aluminosilicate (CMAS) glass.* Journal of the European Ceramic Society, 2015. **35**(10): p. 2907-2914.
28. Zhao, H., C.G. Levi, and H.N.G. Wadley, *Molten silicate interactions with thermal barrier coatings.* Surface and Coatings Technology, 2014. **251**: p. 74-86.
29. Dingwell, D.B., *Viscosity-temperature relationships in the system $Na_2Si_2O_5$-$Na_4Al_2O_5$.* Geochimica et Cosmochimica Acta, 1986. **50**(6): p. 1261-1265.
30. Webb, P.A. et al., *Analytical methods in fine particle thechnology.* Micromeritics Instrument Corp., 1997: p. 53-218.
31. Giordano, D., J.K. Russell, and D.B. Dingwell, *Viscosity of magmatic liquids: A model.* Earth and Planetary Science Letters, 2008. **271**(1): p. 123-134.
32. Renteria, A.F., et al., *Effect of morphology on thermal conductivity of EB-PVD PYSZ TBCs.* Surface and Coatings Technology, 2006. **201**(6): p. 2611-2620.
33. Flores Renteria, A., *A small-angle scattering analysis of the influence of manufacture and thermal induced morphological changes on the thermal conductivity of EB-PVD PYSZ thermal barrier coatings*, in *Fakultät für Georessourcen und Materialtechnik*. 2007, RWTH Aachen University. p. 151.
34. Song, W., et al., *Wetting and spreading of molten volcanic ash in jet engines.* The Journal of Physical Chemistry Letters, 2017. **8**(8): p. 1878-1884.
35. Naraparaju, R., et al., *Interaction and infiltration behavior of Eyjafjallajökull, Sakurajima volcanic ashes and a synthetic CMAS containing FeO with/in EB-PVD ZrO_2 -65 wt% Y_2O_3 coating at high temperature.* Acta Materialia, 2017. **136**: p. 164-180.
36. Koch, K., et al., *Fabrication of artificial Lotus leaves and significance of hierarchical structure for superhydrophobicity and low adhesion.* Soft Matter, 2009. **5**(7): p. 1386-1393.
37. Jung, Y.C. and B. Bhushan, *Contact angle, adhesion and friction properties of micro-and nanopatterned polymers for superhydrophobicity.* Nanotechnology, 2006. **17**(19): p. 4970.
38. Poirier, D.R. and G.H. Geiger, *Transport phenomena in materials processing*. 1994, Warrendale, Pa.: Minerals, Metals & Materials Society.
39. Kucuk, A., A. Clare, and L. Jones, *An estimation of the surface tension for silicate glass melts at 1400° C using statistical analysis.* Glass Technology, 1999. **40**(5): p. 149-153.
40. Lavinge, O., et al., *Influence of morphology on thermal properties and CMAS resistance of gadolinium zirconate EB-PVD coatings*. 2016: Poster presented at HELSMAC symposium, Cambridge.
41. Jackson, R.W., et al., *Interaction of molten silicates with thermal barrier coatings under temperature gradients.* Acta Materialia, 2015. **89**: p. 396-407.
42. Poerschke, D.L., R.W. Jackson, and C.G. Levi, *Silicate Deposit Degradation of Engineered Coatings in Gas Turbines: Progress Toward Models and Materials Solutions.* Annual Review of Materials Research, 2016. **46**: p. 235-262.

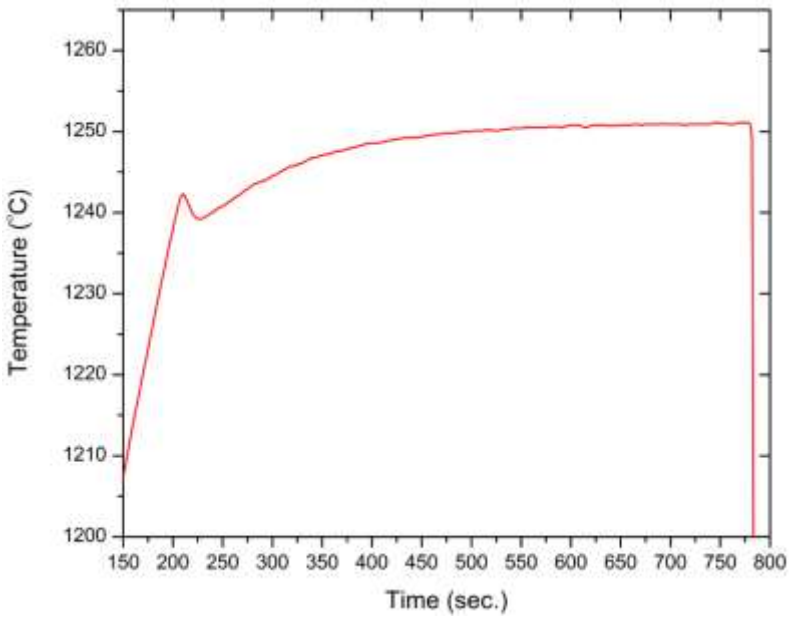

Figure 1

Heating profile plot for the CMAS infiltration testing at 1250°C. The time required to reach 1250°C is about 8 min. (480 seconds). The testing time at a constant temperature of 1250°C after this ramp-up was changed from 30 seconds up to 8 min., followed by rapidly forced air-cooling to room temperature as seen from the sudden temperature drop at the end.

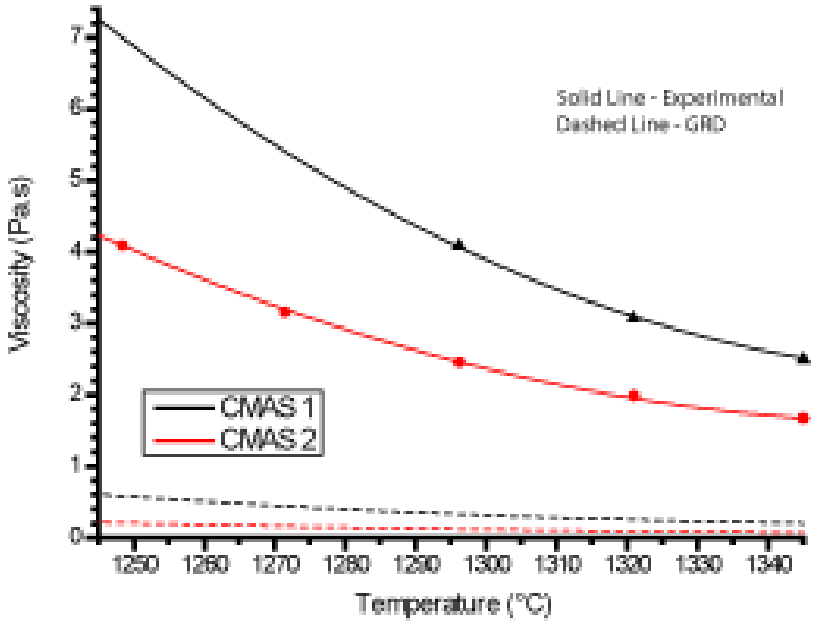

Figure 2

Viscosities for CMAS 1 and CMAS 2 measured experimentally (solid lines) and calculated data using the GRD model [33] (dashed lines) at different temperatures.

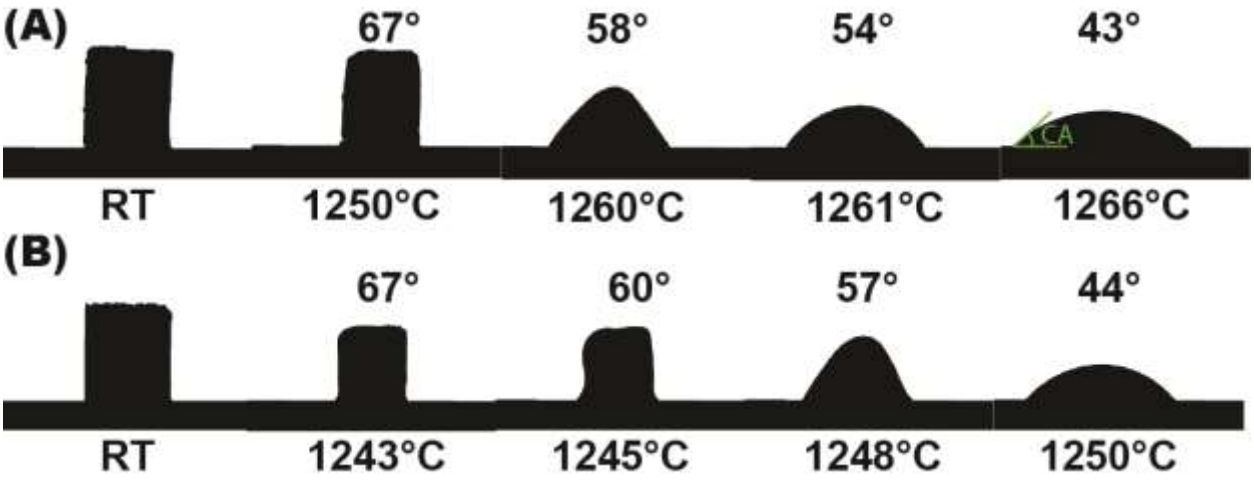

Figure 3

Imaging from heating microscope for (A) CMAS 1 and (B) CMAS 2 on alumina substrates at different temperatures. RT means room temperature. The CA mark shows the measured contact angle by the imaging software.

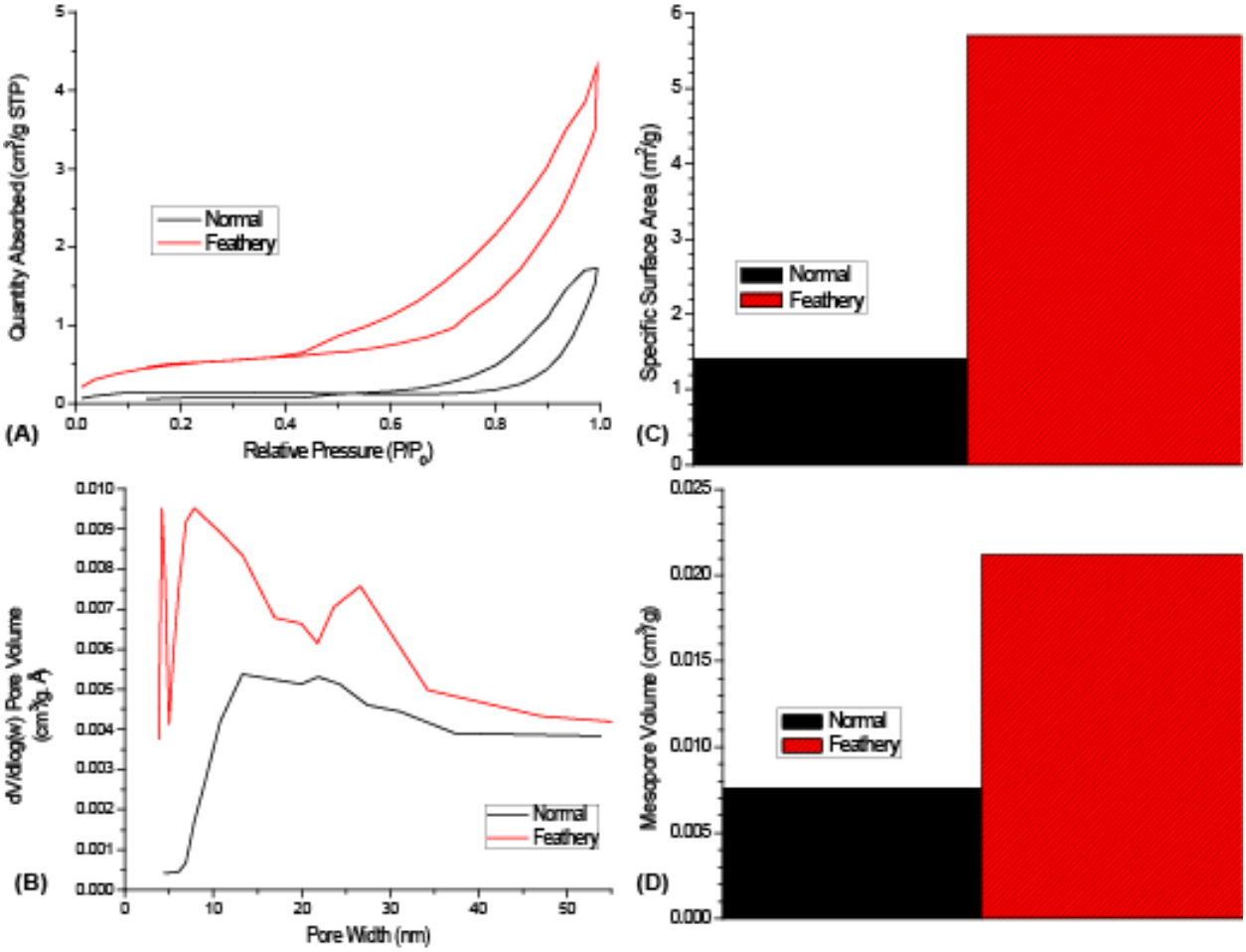

Figure 4

Pore fraction measurements for ‘normal’ and ‘feathery’ TBCs. A) nitrogen absorption for each microstructure, b) the pore volume, c) details specific surface area, and d) gives the volume of mesopores with dimensions between 2 to 50 nm.

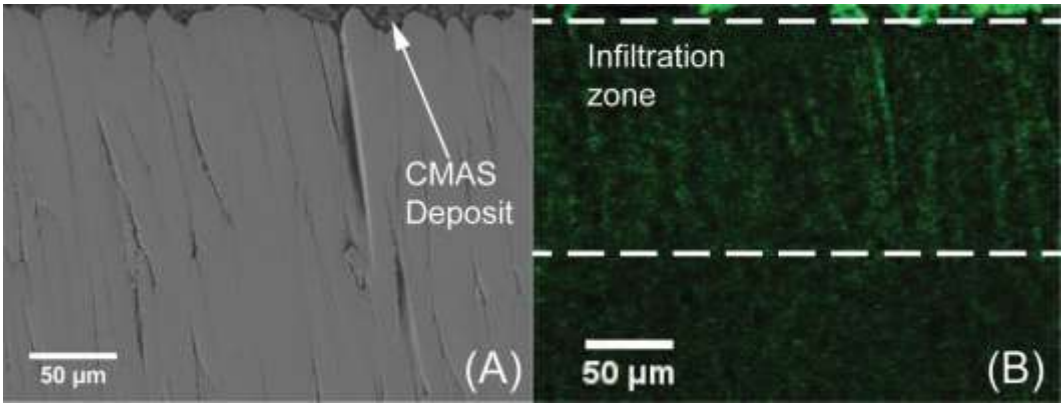

Figure 5

Cross-sectional SEM image of the top portion of the normal 7YSZ TBC for CMAS 1 under 30 seconds infiltration testing at 1250°C (A). Si elemental mapping is shown in green color (B) for the sample. The infiltration zone is delimited within the white dotted lines.

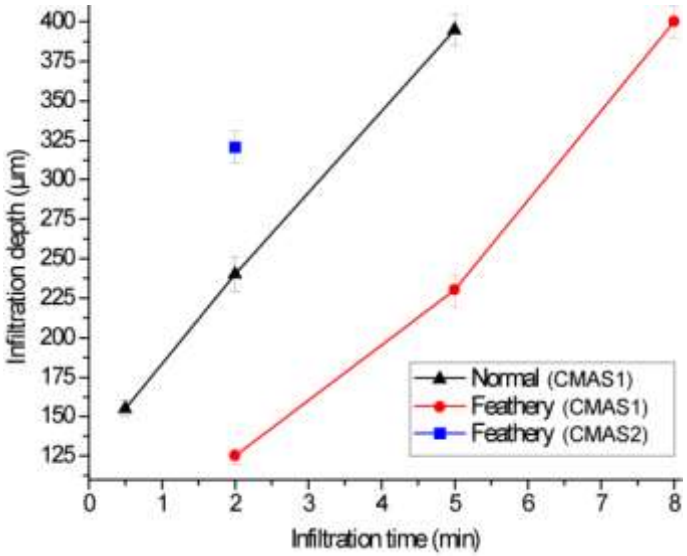

Figure 6

Experimentally measured infiltration depth for CMAS 1 for ‘normal’ and ‘feathery’ microstructures tested at 1250°C from 30 seconds to 8 minutes. Note that only one data point for CMAS 2 ‘feathery’ after 2 min is provided since the ‘normal’ microstructure was completely infiltrated after the tested time.

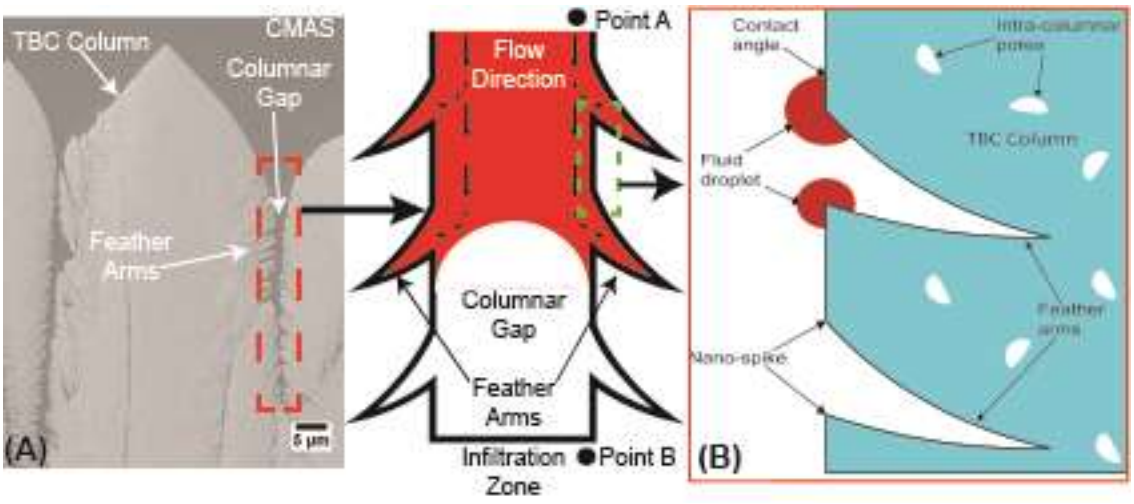

Figure 7

Schematic for the effect of the geometric factor splitting the molten glass flow in the TBC. (A) at the columnar gap section, (B) schematic at the feather arms showing the interaction of fluid droplets with the feather arms generating different contact angles at the inner surfaces of a columnar gap wall.

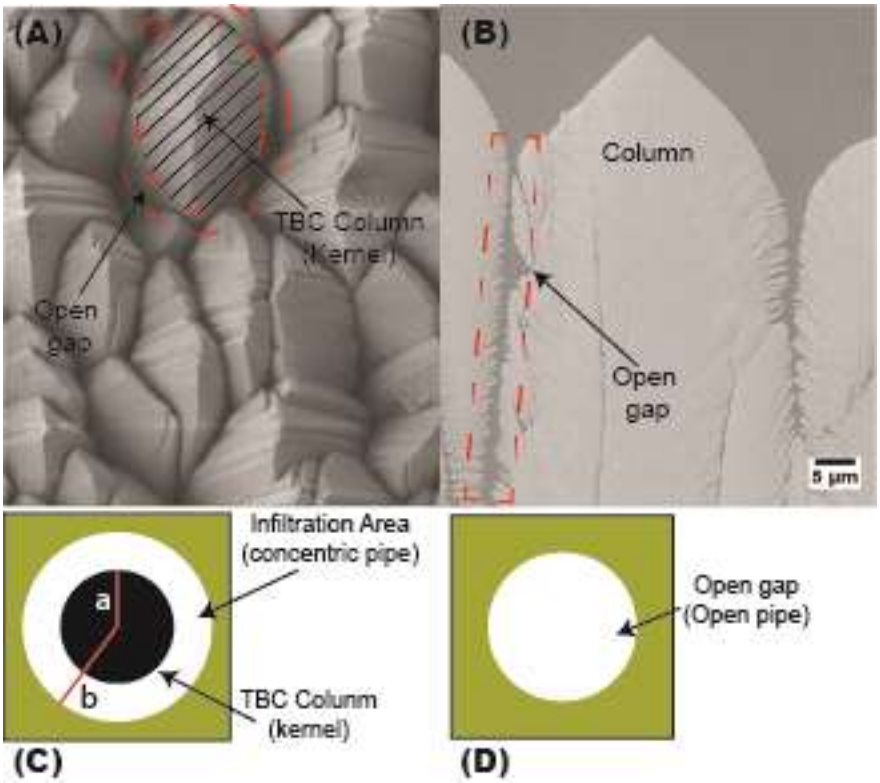

Figure 8

Schematic of the concentric and open pipe models. (A) Top view SEM image showing the distribution of TBC columns and columnar gaps. The shadowed area shows the TBC column

(kernel) and the circled area represents the columnar gap (concentric pipe) open for infiltration. (B) Cross sectional SEM image showing the single open gap (open pipe) for infiltration in the red dashed rectangle. (C) Simple representation of the concentric pipe with the kernel inside with their respective radius a and b. (D) Simple representation of the open pipe radius considered in the open pipe model.

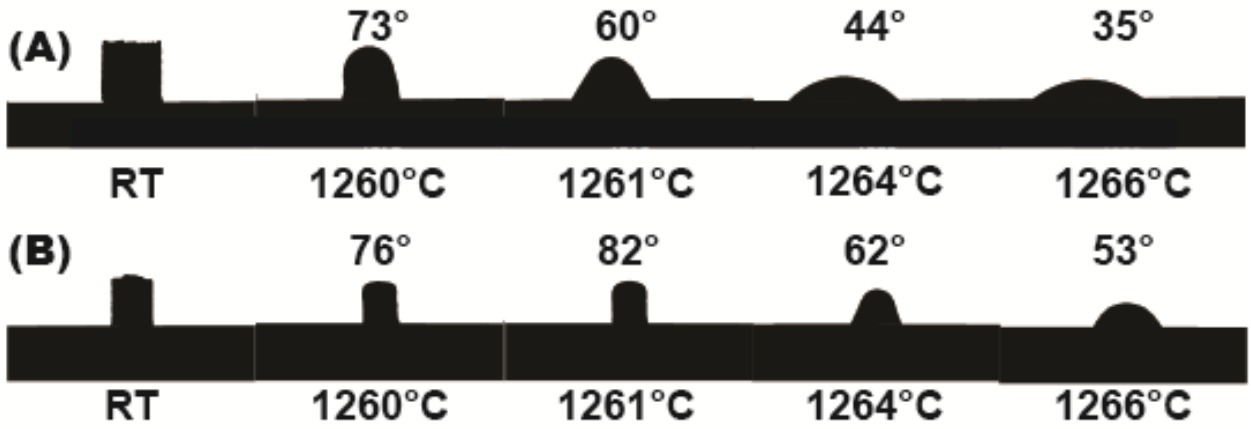

Figure 9

Imaging from heating microscope for CMAS 1 on top of TBC coated samples with (A) ‘normal’ and (B) ‘feathery’ microstructures at different temperatures.

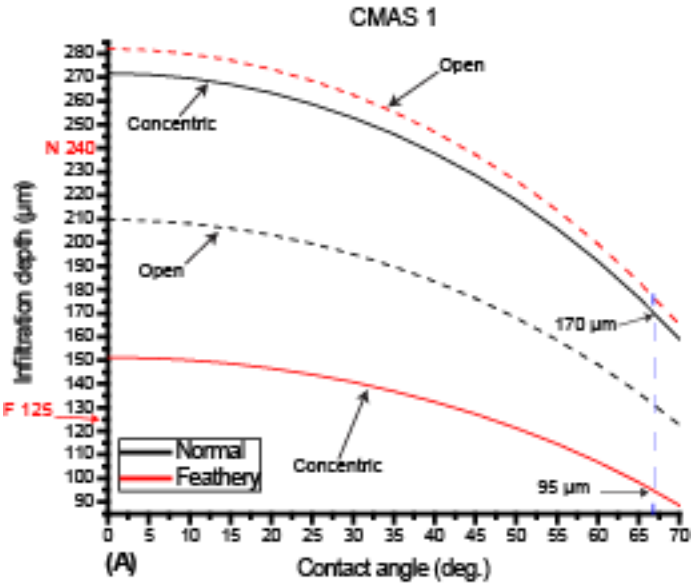

Figure 10a

Prediction of CMAS 1 infiltration with respect to change in contact angle for concentric (solid lines) and open pipe (dashed lines) models including ‘normal’ and ‘feathery’ microstructures. The experimentally measured infiltration depth for both microstructures is marked at the infiltration axis (Y) in red color. The blue dashed line represents the measured contact angle for CMAS 1 at 1250°C (67).

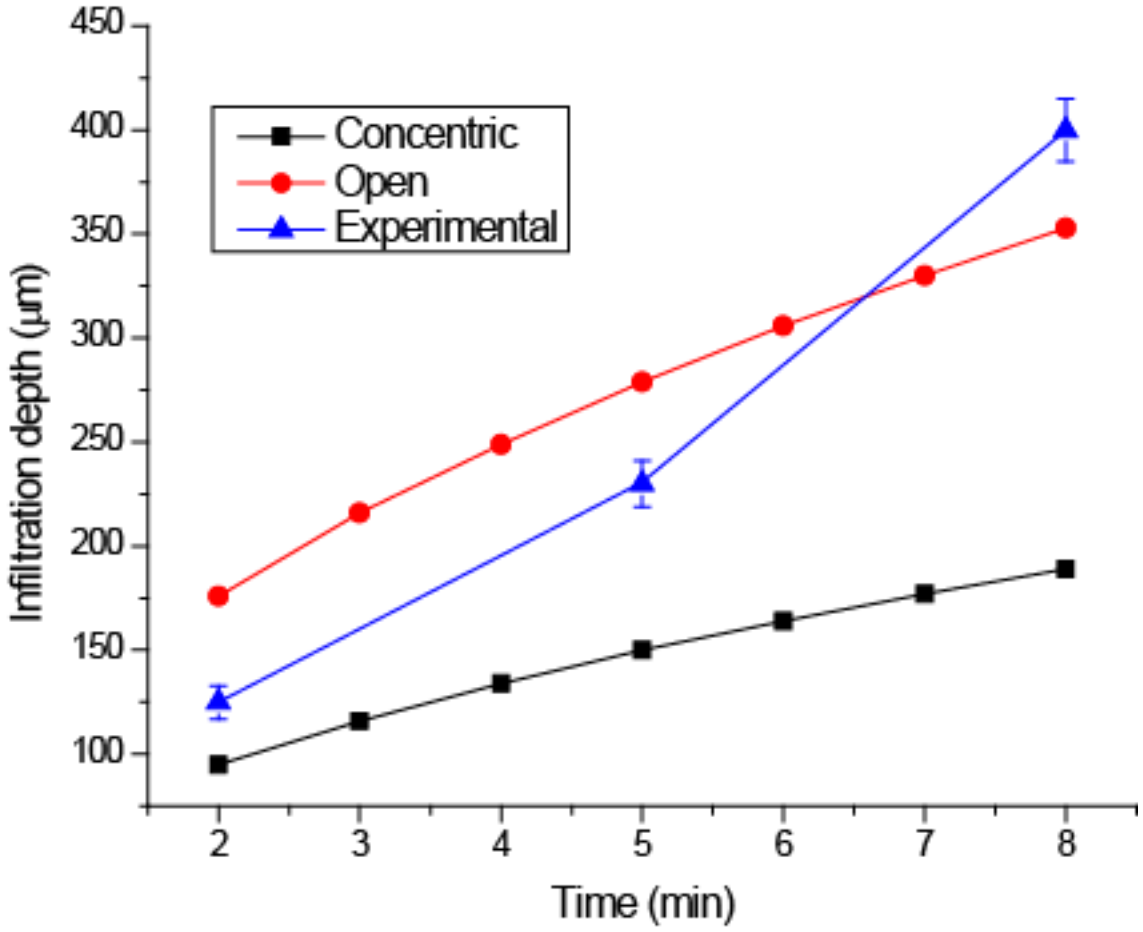

Figure 10b

Predicted CMAS 1 infiltration for the feathery microstructure with respect to time vs experimental infiltration. The predicted values are calculated with a contact angle of 67˚.

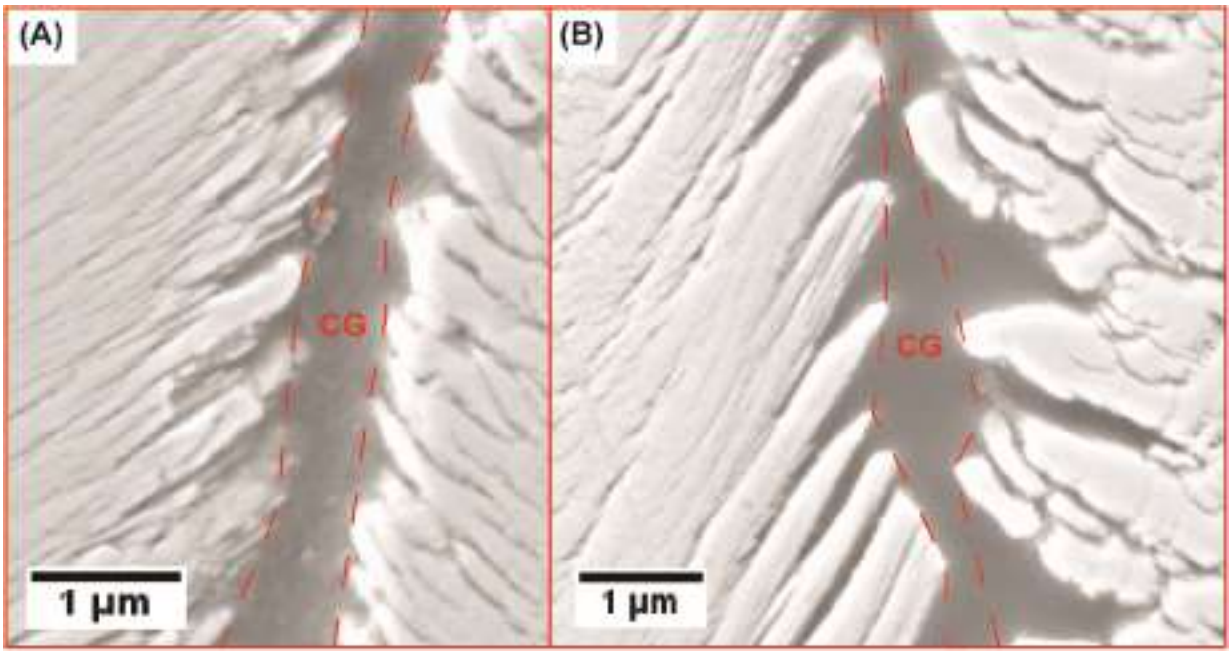

Figure 11

Example of an SEM imaging section used for geometric factor estimation for (A) ‘normal’ and (B) ‘feathery’ microstructure of 7YSZ EB-PVD TBCs.

Table 1

Summary of microstructural features for ‘normal’ and ‘feathery’ microstructures.

Morphology	Porosity (%)	Colunm width (μm)	Gap width (μm)
Normal	14.5	18.5	2
Feathery	29.5	11.5	1.1

Table 2

Summary of the chemical composition in mol. % and melting behaviors for CMAS 1 and 2.

	CMAS 1	CMAS 2[δ]
Stoichiometry	(Mol. %)	(Mol. %)
SiO_2	41.7	38.2
CaO	24.6	30.9
MgO	12.4	11.4
Al_2O_3	11.0	10.1
FeO	8.7	8.0
TiO_2	1.6	1.4
Melting Onset (°C)	1215-1225	1200-1210
Melting Point (°C)	1258-1265	1243-1250

[δ] Normalized composition to non-volatile components

Table 3

Fluid properties for CMAS 1 and 2 including experimental and predicted viscosities, contact angle at 1250°C and estimated surface tension.

	Viscosities (Pa.s)		(deg.)	(J/m^2)
	GRD	Exp.	Contact Angle	Surface Tension
CMAS 1	0.6	6.9	67	0.44
CMAS 2	0.2	4.0	44	0.46

Table 4

Summary of infiltration depth for CMAS 1 after 120 seconds at 1250°C. Measured data by SEM are compared with the concentric and open pipe models using measured and calculated (GRD) viscosity. The results are included for 'normal' and 'feathery' microstructures.

CMAS 1

Sample	Infiltration depth (μm)	Experimental infiltration time (sec.)	Concentric pipe (μm)		Open pipe (μm)	
			Experimental viscosity	Giordano viscosity	Experimental viscosity	Giordano viscosity
Normal	240	120	170	590	131	455
Feathery	125	120	95	329	176	613

Table 5

Summary of infiltration depth for CMAS 2 after 120 seconds at 1250°C. Measured data by SEM are compared with the concentric and open pipe models using measured and calculated (GRD) viscosity. The results are included for 'normal' and 'feathery' microstructures.

[1]Note that the infiltration time is higher for the CMAS 2 case which counts for the 210 seconds extra that the system requires to reach 1250 degrees from the melting point of 1243 degrees.

CMAS 2

Sample	Infiltration depth (μm)	Experimental infiltration time (sec.)	Concentric pipe (μm)		Open pipe (μm)	
			Experimental viscosity	Giordano viscosity	Experimental viscosity	Giordano viscosity
Normal	Full	330[1]	515	2307	397	1779
Feathery	320	330[1]	286	1284	534	2395